Full length article

Enhanced energy storage density in Sc^{3+} substituted $Pb(Zr_{0.53}Ti_{0.47})O_3$ nanoscale films by pulse laser deposition technique

Mohan K. Bhattarai[a], Karuna K. Mishra[a], Alvaro A. Instan[a], Bishnu P. Bastakoti[b,*], Ram S. Katiyar[a,*]

[a] Department of Physics, University of Puerto Rico, P. O. Box 70377, San Juan, PR 00936-8377, USA
[b] Department of Chemistry, North Carolina A&T State University, 1601 East Market Street, Greensboro, NC 27411, USA

A B S T R A C T

Highly oriented $Pb(Zr_{0.53}Ti_{0.47})_{0.90}Sc_{0.10}O_3$ (PZTS) thin films were deposited on $La_{0.67}Sr_{0.33}MnO_3$ (LSMO) buffer layer coated on MgO (100) substrates by following two subsequent laser ablation processes in oxygen atmosphere employing pulse laser deposition technique. The PZTS films were found to grow in tetragonal phase with orientation along (100) plane as inferred from x-ray diffractometry analysis. The structural sensitive symmetric E (LO_2) Raman band softened at elevated temperature along with its intensity continuously decreased until it disappeared in the cubic phase above 350 K. The existence of broad Raman bands at high temperature (> 350 K) is attributed to the symmetry forbidden Raman scattering in relaxor cubic phase due to symmetry breaking in nano length scale. The temperature dependent dielectric measurements were performed on metal-ferroelectric-metal capacitors in the frequencies range of 10^2–10^6 Hz was observed to be diffused over a wide range of temperature 300–650 K and exhibits high dielectric constant ~5700 at room temperature. An excellent high energy storage density (U_{re}) ~54 J/cm³ with efficiency ~70% was estimated at applied voltage 1.82 MV/cm. High DC breakdown strength, larger dielectric constant and high restored energy density values of our PZTS thin films indicate its usage in high energy storage applications.

1. Introduction

Due to the increasing trend of fossil fuel consumption, it has certainly been anticipated worrisome about future energy supply and its devastating impact on the eco-friendly environment. Therefore, in recent years, researchers have been attempting to find other alternative sources of energy by the development of new technologies for low-cost, high energy storage and power sources [1,2]. Ironically, renewable resources can replace fossil fuels; however, the energy produced from renewable resources is primarily electrical energy, which often introduces the challenge of energy storage. Solving the problem of electrical energy storage is the most challenging prerequisite issue in the possible transition to a renewable energy economy era. Therefore, it is of interest to have better and more efficient solutions as far as electrical energy storage is concerned. In the most recent years, dielectric capacitors with high energy-storage densities have attracted prominent investigation due to their potential application in modern electronics and electrical power systems. In addition, it can be of great choice for electronic applications [3–5] (lasers, wind power generator, and medical defibrillators) as power inverter and a pulsed power source.

Dielectrics materials for high energy densities have been mainly focused on linear dielectric materials (LDs), ferroelectric materials (FEs), Relaxor ferroelectric (RFs) and antiferroelectric materials (AFs). Among these, RFs and AFs are more commonly used dielectric capacitors due to their higher energy storage densities than those of LDs and FEs [3,6–8]. Relaxors behaviors in a ferroelectric are governed by the evolution of polar nanoregions (PNRs), originated from the chemical frustration occurs in a compositionally induced disordered system to maintain charge neutrality [9]. Relaxors ferroelectrics have unique physical properties such as high dielectric constant, broad temperature and dispersive frequency maximum of the dielectric permittivity, the giant piezoelectric effect [10,11]. The slim polarization-electric field (*P-E*) hysteresis loop of relaxor ferroelectrics yields a more substantial area to store the energy and exhibits high discharge capacity [8,12].

Remarkably, the responses of linear dielectric and a nonlinear dielectric such as ferroelectric and/or relaxor-ferroelectric under applied stimulus electric fields can be explained by the behavior of typical polarization *P* and permittivity *ε* with respect to applied electric field *E* (Fig. 1). For these materials, their effective energy density can be determined by the shaded area of the *P-E* diagram (Fig. 1) [8]. The
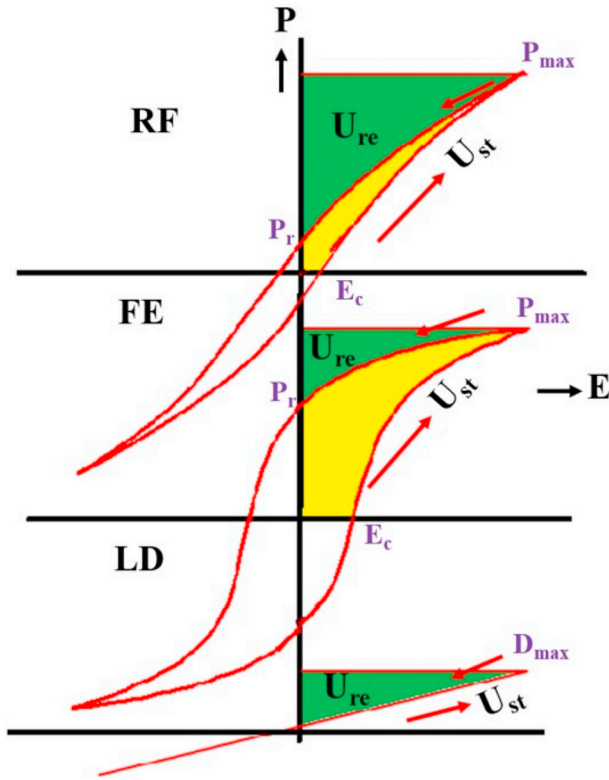
Fig. 1. A schematic diagram of the *P–E* behavior of linear dielectric (LD), ferroelectrics (FE), and relaxor- ferroelectrics (RF) materials.

recoverable electric energy density per unit volume, U_{re}, is released on discharge from E_{max} to zero, represented by the green shaded area in Fig. 1, which can be obtained by integrating [13].

$$U_{re} = \int_{P_{max}}^{P_r} E dP \qquad (1)$$

where E is the applied electric field, P is the displacement charge density for ferroelectric materials, and P_r is the remnant polarization. Similarly, when the electric field increases from zero to the maximum E_{max}, the polarization increases to the maximum P_{max}, and electric energy is stored in the capacitor as U_{st}. One can define the energy storage efficiency η as

$$\eta = \frac{U_{re}}{U_{st}} \times 100\% \qquad (2)$$

The lead zirconate titanate (PZT) in the vicinity of morphotropic phase boundary (MPB) is well studied ABO_3 type perovskite ferroelectric materials. Its properties can be tuned systematically by substituting ions in either on *A*- site (Pb) and/or *B*-site (Zr/Ti), or on both sites of the perovskite to innovate new materials and achieve improved ferroelectric performance. Recent theoretical studies show that higher ionic radii dopant such as La^{3+}, Nd^{3+}, Ta^{5+} (donor dopant), enter into *A*-site whereas that of lower ionic radii such as Sc^{3+}, Yb^{3+}, and Fe^{3+} ions (acceptor dopant) occupy at *B*-site, results in strengthen of domain wall mobility and enhances electronic properties of PZT [14]. Several investigations have shown La^{3+} doped PZT is a very good relaxor material for high energy storage application [3,5,15,16]. For instance: $Pb_{0.97}Y_{0.02}[(Zr_{0.6}Sn_{0.4})_{0.925}Ti_{0.075}]O_3$ exhibited $U_{re} = 21.0 \, J/cm^3$ with a high energy-storage efficiency of η = 91.9% under an electric field of 1.3 MV/cm [7]. Epitaxial PLZT thin film capacitors showed a recoverable energy density (U_{re}) ~31 J/cm^3 for the applied field of ~2.3 MV/cm [17]. An examination on this material up to 10^8 (measured) charge-discharge cycles found that a larger polarization-fatigue endurance capacity, an important parameter for the application of

ferroelectric capacitors, is maintained [18–20]. Sol-gel based highly (100)-oriented doped $(Pb_{1-x-y}La_xCa_y)Ti_{1-x/4}O_3$ (x = 0.1 & y = 0.1) thin films exhibit relaxor behavior and possessed U_{re} ~15 J/cm^3 [21]. A and B-site doped $(Bi_{0.5}Na_{0.5})TiO_3–Bi(Ni_{0.5}Zr_{0.5})O_3$ relaxor exhibits a better energy storage density $U_{re} = 50.1 \, J/cm^3$ with an energy-storage efficiency of 63.9% [22]. *B*-site doped Sc^{3+} is found to improve the endurance capacity of PZT materials [23]. Importantly, the reduction of remnant polarization P_r has been reported due to the off-center Sc^{3+} ions substitution and resulting in a slim P-E loop [24]. Role of Sc^{3+} doping on B-site is reported to improve the relaxor behaviors in $Pb_{0.78}Ba_{0.22}Sc_{0.5}Ta_{0.5}O3$ [25] and $PbSc_{0.5}Nb_{(1-x)/2}Ta_x/2O_3$ (PSNT) with $0 \leq x \leq 1$ [26]. Therefore, *B*-site substitution of Sc^{3+} on PZT is expected to improve the relaxor behavior of doped compound and consequently, acts as a high energy storage density capacitor; which has to be examined. Interestingly, the recoverable energy density, high energy efficiency, and piezoelectric strain were found to enhance by the substitution of rare earth elements like Sc^{3+} [27]. In thin films, one dimension is reduced in nano-scale, result in a significant improvement in breakdown electric field [12,28] and hence, a higher energy storage density ($U_{st} = ½ \, CV^2$) is realized in quasi-two-dimensional materials like thin films. Therefore, it is of interest to grow Sc^{3+} doped PZT ferroelectric in thin films and examine its energy storage capacity and compare with other reported similar systems. Raman spectroscopy is a sensitive technique for identifying phase transitions and short-range ordering in ferroelectric materials [29]. Since the temperature influences the crystal structure and ferroelectric behavior, the vibrational spectra are also expected to be modified. Therefore, it is of interest to examine the thermal induced changes in the phonon spectra and correlate with the dielectric results. Such a study is expected to improve the understanding of ferroelectric behavior in [Pb $(Zr_{0.53}Ti_{0.47})_{0.90}Sc_{0.10}O_3$] (PZTS). In the present work, we focus on the fabrication and investigation of dielectric, electrical, and ferroelectric properties of Sc^{3+} doped epitaxial PZT thin films grown on a conducting metal oxide layer of $La_{0.67}Sr_{0.33}MnO_3$(LSMO) deposited on a MgO (100) substrate using PLD technique. Phase formation of the prepared thin films was checked using X-ray diffractometer. Smooth morphology of the thin films was inferred using Atomic force microscopy. EDX results suggest the stoichiometric of all cationic elements present in the films. The phonon spectra in PZTS are examined as a function of temperature down to 80 K and its possible correlation to observe tetragonal-cubic phase transition and relaxor behavior at elevated temperature are discussed. Temperature-dependent dielectric measurements on PZTS capacitor suggest a diffuse phase transition. Using the P-E hysteresis loop data, the high energy storage density (U_{re}) and efficiency (η) were estimated. Based on our improved results such as high dielectric constant, larger breakdown electric field, slim hysteresis loop, and higher energy storage density U_{re}, the capacitors Pt/ PZTS/LSMO could be a promising material for high energy storage application.

2. Experimental

PZTS/LSMO thin films were grown using a KrF excimer laser (λ = 248 nm, f = 5 Hz) in an oxygen environment ($P_{O2} = 140$ mTorr) on MgO (100) substrates using thin film growth technique by PLD [12,30]. The PZTS target was prepared using the solid-state reaction method following the procedures reported elsewhere [12,24]. The fabrication of thin films using PLD technique were carried out following these multiple steps: (i) laser radiation interaction with the target; (ii) the formation of plasma plume and transportation towards the substrate; (iii) interaction of ablated species with the substrate; and (iv) nucleation and growth of thin film on the surface of the substrate [30]. The optimized PLD deposition parameters for the PSZT thin films are summarized in Table 1. The thicknesses of PZTS thin films were probed using an XP-200 profilometer.

The phase purity and orientation of these prepared thin films at

Table 1
Optimized thin films deposition parameters.

Substrate	MgO (100)
Target	PZTS
Target diameter	0.025 m
Substrate target distance	0.05 m
Growth temperature	873 K
Base vacuum	$\sim 10^{-6}$ Torr
O_2 partial pressure	140 mTorr
Laser source	excimer (λ = 248 nm & f = 5 Hz)
Laser energy used	250 mJ
Repetition rate	10
Total number of shots	3000
Plume energy	150 mJ
Post deposition ex-situ annealing	973 K for 1 h

room temperature were examined by using x-ray diffraction (XRD) employing CuK$_\alpha$ radiation with wavelength λ = 1.5405 Å. Raman spectroscopic measurements were carried out using a HORIBA Jobin Yvon *micro*-Raman spectrometer (model: T64000) equipped with a 50 X long-working distance objective. The acquisition of spectra was carried out in back-scattering geometry using the 514.5 nm line of a coherent Ar$^+$ ion laser (Innova 70-C). Raman spectra were collected at elevated temperature in the *T*-range from 80 K to 580 K using a Linkam heating-cooling stage ensuring temperature stability of ± 1 K. The data were analyzed using damped harmonic oscillator model to determine the spectral parameters: band frequency, linewidth, and intensity. The stoichiometric of the chemical compositions were examined using energy dispersive x-ray analysis results. Atomic force microscopy (AFM-Veeco) was used to know surface morphology and surface roughness of these grown films operated in contact mode. Ambient Piezo force microscopy (PFM) investigations were carried out employing a Multimode Nasoscope (Veeco Instruments) operated using the conductive tips coated with Pt/Ir. The applied driving voltages on the surface of the thin film were ± 12 V. Fabrication of PZTS capacitor sandwiched between conducting bottom LSMO and top Pt electrodes were carried out. Metal shadow mask of an area of 10^{-8} m^2 was used to fabricate Pt square capacitors as a top electrode by DC sputtering (Fig. 2) followed by annealing at 673 K for 20 min with rate 20 K/min in an oxygen atmosphere to compensate oxygen deficiency. We used profilometer to find out the exact area of Pt electrodes and obtained a diffused area in an average $\sim 2 \times 10^{-8}$ m^2. The temperature dependent dielectric behaviors at various frequencies (100 Hz-1 MHz) were carried out using an HP4294A impedance analyzer & MMR Technologies K-20 programmable temperature controller. The room temperature ferroelectric hysteresis curves (*P-E* loops) were measured using Radiant tester set up.
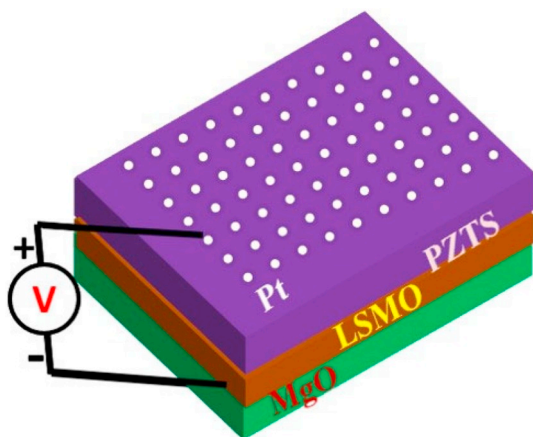
Fig. 2. Fabrication of PZTS capacitor sandwiched between conducting bottom LSMO and top Pt electrode.
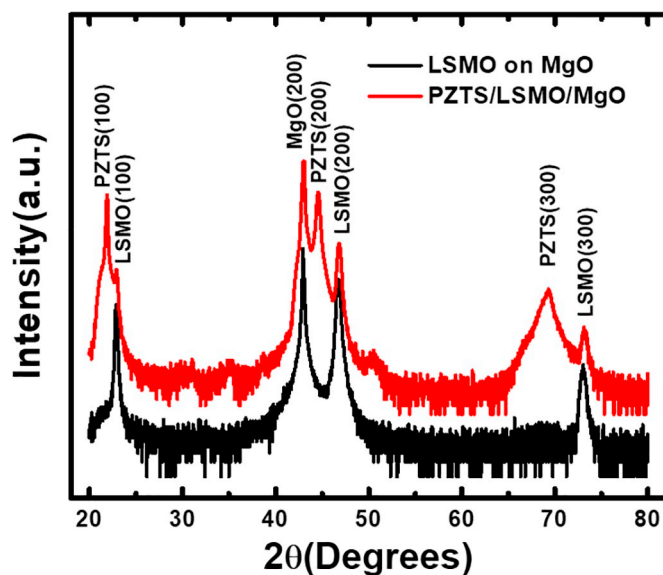
Fig. 3. Room temperature XRD Bragg peaks of PZTS thin films. The PZTS reflections peaks are also labelled.

3. Results and discussion

3.1. Structural and microstructural results

XRD pattern measured from PZTS thin films grown on highly oriented (100) MgO substrates by using the PLD technique is shown in Fig. 3. It indicates the formation of a single-phase perovskite structure with preferential (100) orientation parallel to the film surface. The diffraction peaks located at 2θ $\sim$21.89, 44.57 and 69.53 correspond to (100), (200), and (300) planes of tetragonal structure, and observation of a slight distortion in crystal structure due to scandium doping (JCPDF: 33–0784) at room temperature is noticed. The diffraction peak position (2θ) of (100) reflection was obtained by fitting with a Gaussian profile function, and the lattice parameter was estimated as a$_{film}$ = 0.406 nm, slightly smaller than that in PZTS ceramics (Fig. S1) (a$_{bulk}$ = 0.406 nm and c$_{bulk}$ = 0.409 nm for tetragonal symmetry space group P4mm). In our PZTS thin film, in-plane lattice strain of 0.24% was estimated using the equation, $s = \frac{a_{bulk} - a_{film}}{a_{bulk}} \times 100\%$, attributed to lattice mismatch across the substrate/electrode/film interface or thermal annealing [11].

AFM micrograph (inset: Fig. 4) obtained from the surface of the thin films show a smooth surface topography throughout the surface of the sample with root mean square roughness value of $\sim$3 nm, comparatively an improved in roughness value from those reported in PZT films deposited on ITO-coated substrates [31]. The thickness of the thin films is found to be around $\sim$340 nm estimated using Profilometer profile. Fig. 4 exhibits EDX (inset: AFM image) spectrum of the different composition excited by an electron beam of energy 20 kV, showing the presence of elements (Pb, Zr, Ti, Sc and O) at room temperature, along with their respective characteristic x-ray emission lines (O Kα 0.525 keV, Zr Lα 2.042 keV, Sc Kα 4.089 keV, Ti Kα 4.508 keV, Pb Mβ 5.076 keV and Pb Lα 10.552) which is in good agreement with the theoretical emission line spectra.

3.2. Dielectrics behavior

Fig. 5 shows the variation of relative dielectric permittivity (ε) of the thin film at different frequencies. At room temperature PZTS thin films have dielectric constant (ε) $\sim$5700 and loss tanδ $\sim$0.01 measured at frequency 100 Hz. We observed enhanced dielectric constant (ε′) of PZTS thin films as compared to pure PZT [32,33]. A strong frequency
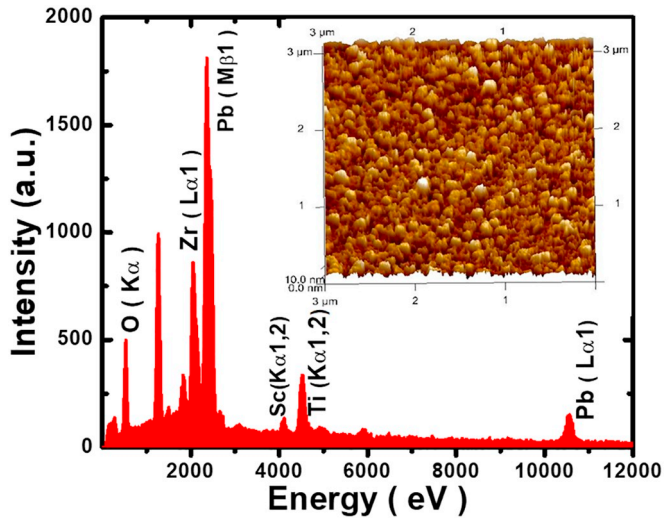
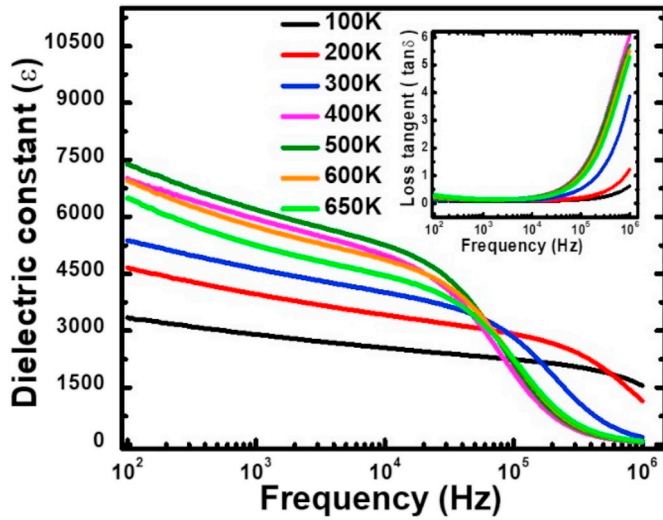**Fig. 4.** EDX spectrum of PZTS thin films (inset: AFM image).

Fig. 5. Frequency dependencies of dielectric constant (ε) of PZTS thin film at different temperature (inset: dissipation factor (tanδ) with frequencies).

dispersion with a significant decay in dielectric constant above 10^5 Hz is found, while ε_r was observed to be stable below the 10^5 Hz frequency. The present dielectric behavior is similar to that observed in other studied ferroelectrics such as $Pb(Zr_{0.2}Ti_{0.8})_{0.70}Ni_{0.30}O_{3-\delta}$ [34], $Pb_{1-x}Sm_x (Zr_{0.55}Ti_{0.45})_{1-x/4}O_3$ ($x = 0.00$–0.09) [35]. The loss tangent in the frequency range 10^2 to 10^4 Hz is almost constant ≤ 0.10 followed by a drastic increment in its trend was seen above 10^5 Hz (inset: Fig. 5). The low dielectric constant and larger loss at a higher frequency is argued to be due to the semiconducting nature of the bottom electrode and its response to the probe frequency [36]. As shown in Fig. 6(a) inset, a diffuse permittivity peak with strong frequency dispersion is observed around 450 K, where the permittivity decreases and the maximum permittivity temperature (T_m) shift towards higher temperature with increasing frequency, typical behavior of a relaxor ferroelectric. Therefore, the frequency dependency with T_m can be explained by using Vogel-Fulcher relation which is represented by equation [37]. Fig. 6a shows the lnf vs. $1000/T_m$ in the frequency ranges 1–40 kHz and analyzed using the following equation.

$$f = f_0 exp\left[\frac{-E_a}{k_B(T_m - T_{VF})}\right]$$

(3)

where the fitting parameters such as f_0 is the pre-exponential factor, E_a is the activation energy, and T_{VF} is the characteristic Vogel-Fulcher freezing temperature. k_B is Boltzmann's constant [38,39]. The fitting yields $E_a = 0.037$ eV in the same order as reported for $Pb(Zr_{0.53}Ti_{0.47})_{0.6}(Fe_{0.5}Ta_{0.5})_{0.4}O_3$ [11], $f_0 = 1.538 \times 10^6$ Hz, a physically acceptable value [40] and $T_{VF} = 397$ K. Besides this, the dielectric permittivity of a ferroelectric can be explained by the well-known Curie-Weiss law above the T_m region, which is given by [41,42].

$$\frac{1}{\varepsilon} = \frac{T - T_m}{C} (T > T_m),$$

(4)

where C is the Curie-Weiss constant. The plot of the temperature dependence of inverse dielectric constant of PZTS at 30 kHz, is shown in Fig. 6(b), fitted to the Curie-Weiss law. The value of C is found to be 27.93×10^5, in the same order as reported for other relaxor ferroelectrics [12,43]. The difference in temperature $\Delta T_m = T_{CW} - T_m$ is ~90 K, where T_{cw} indicating the temperature where the deviating of Curie-Weiss law begins, and T_m is the temperature corresponding to the dielectric maximum. The fitted parameters are listed in Table 2. This differences in temperature ΔT_m represent the degree of deviation from the Curie-Weiss law and provides evidence of a compositional-induced diffuse phase transition at elevated temperature in PZTS [12,44].
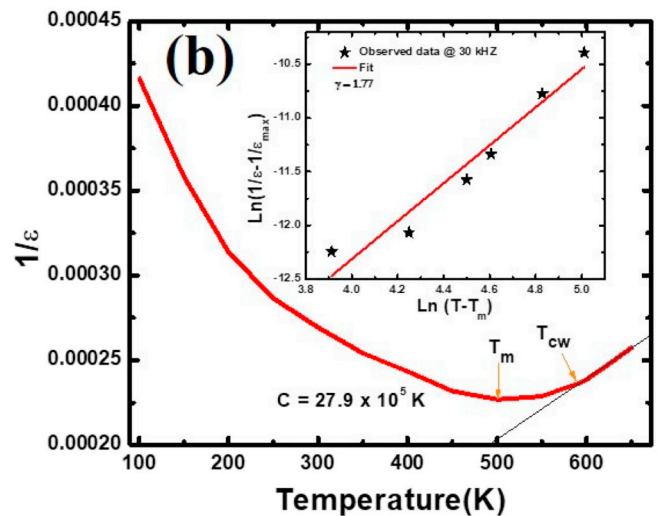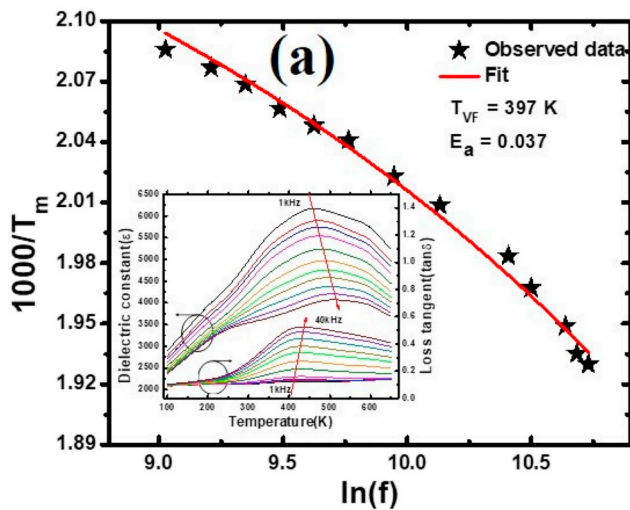

Fig. 6. (a) Vogel Fulcher relation [inset: temperature dependencies of the dielectric constant (ε) of the PZTS thin films at different frequencies and variation of loss tangent] (b). Reciprocal of dielectric constant (1/ε) with the temperature at 30 kHz frequencies (inset: modified Curie Weiss law plot at 30 kHz).

Table 2
Summary of parameters of PZTS relaxor ferroelectric.

Parameter	ε_m	T_m (K)	C (K)	T_{cw}(K)	ΔT_m (K)	γ
Fitted values	4408	500	27.9×10^5	590	90	1.77

Moreover, the dielectric characteristics and the diffuseness of the ferroelectric phase transition can be interpreted by a modified Curie-Weiss law [45,46].

$$\frac{1}{\varepsilon} - \frac{1}{\varepsilon_m} = \frac{(T - T_m)^\gamma}{C'} \ (1 \le \gamma \le 2), \tag{5}$$

where C′ is Curie Weiss like constant. The value of the other fitting parameter γ gives information on the nature of the phase transition. For γ = 1, a normal Curie- Weiss law is obtained and is expected for a normal ferroelectric, whereas γ = 2 describes a complete diffuse phase transition [47]. The γ value between 1 < γ < 2 suggests an incomplete diffuse phase transition in the ferroelectric where the polar nanodomains are correlated in a non-polar matrix. The behavior of ln $(T - T_m)$ versus $\ln\left(\frac{1}{\varepsilon} - \frac{1}{\varepsilon_m}\right)$ obtained from 30 kHz, as shown in the inset of Fig. 6b, is analyzed by a linear equation. The slope of the linear relationship gives the value of γ as 1.77. The value of γ clearly indicates the diffuse phase transition in PZTS. The observed diffuseness in the plot of temperature against dielectric permittivity (ε) (Inset: Fig. 6a) is one of the significant behavior of the compositionally disordered materials exhibiting a diffuse phase transition [48,49].

3.3. Raman spectroscopic studies

We now discuss the phonon spectra in PZTS. As mentioned earlier, the substitution of Sc^{3+} cation resulted in a tetragonal structure (*P4mm*) of PZTS with reduced tetragonal lattice distortion. The irreducible representation of normal optical phonons in the ambient phase is $\Gamma_{opt} = 3A_1 + 4E + B_1$, where the A_1 and E modes are both Raman active and infra-red active, while B_1 mode is only Raman active. The polar infrared active A_1 and modes E are further split into LO-TO modes because of long-range coulombic interaction forces among cations. Fig. 6a shows the Raman spectrum of PZTS measured at ambient temperature in the frequency range 60–1000 cm^{-1}. Six prominent Raman bands located at 294, 425, 481, 573, 715, and 786 cm^{-1} are identified by analyzing the spectrum. These band frequencies are found to be similar to those reported for tetragonal PZT [50] and are assigned by comparing with those reported mode frequencies (Fig. 7). Except for the E(LO$_2$) band at 425 cm^{-1}, all other bands are found to be broader as compare to tetragonal ferroelectric PbTiO$_3$ compound [51]. The broadening of these bands could be due to several factors: finite temperature effect has an inherent contribution to broadening since the phonon lifetime decreases with temperature. Another factor for broadening is due to substitutional disorder, as is known to have a significant contribution to the inhomogeneous broadening, [52] originating from the statistical distribution of bond lengths related to change in bond strength of different cations at *B*-sites of PZTS. Appearance of A$_1$(TO$_1$) Raman band which represent the vibration of Ti/Zr atoms against O and Pb cations and A$_1$(TO$_3$) band consists of displacement of Zr/Ti and O atoms along c-axis suggest the existence of ferroelectric ordering in PZTS.

Fig. 8(a) shows the Raman spectra measured as a function of temperature in the *T*-range 80–550 K. The spectrum at 80 K, the lowest temperature of the present study, has the similar spectra features as observed at ambient, except that the Raman bands located at 294, 573, and 715 cm^{-1} become stronger and appear as broad band. The symmetric E(LO$_2$) band at 425 cm^{-1} is found to be relatively sharpening at low temperature. The broadening of peaks even at lowest temperature is due to substitutional disorder at *B*-site by Zr, Ti, and Sc cations. Upon
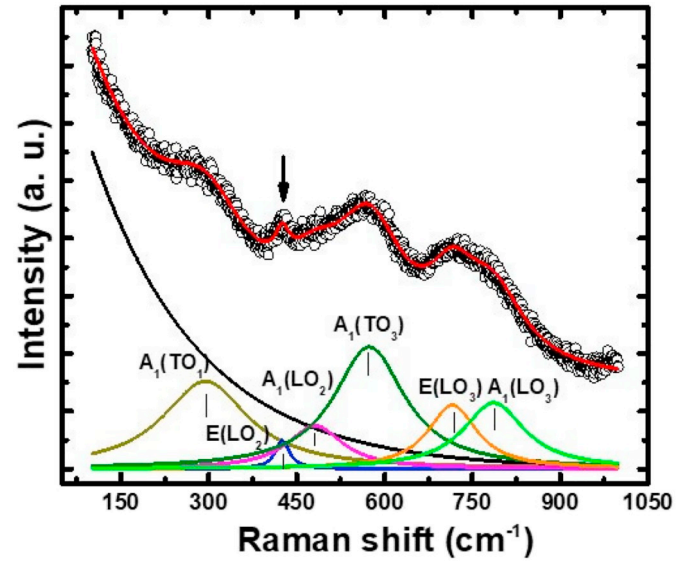

Fig. 7. Raman spectrum measured at 298 K, analyzed using sum of six Lorentzian peaks for PZTS compound. Individual Raman bands are also shown. The Raman bands are assigned as compared to those for tetragonal ferroelectric PZT.

increasing temperature, the spectra broaden further, and their intensities are observed to decrease. Only the broad bands at 573 and 715 cm^{-1} are survived up to as high as 550 K, the highest temperature. Other bands could not be followed up possibly due to an insufficient intensity of weak bands. The symmetric and distinct E (LO$_2$) Raman bands are found to soften at elevated temperature, intensity continuously decreases and vanishes at 350 K (Fig. 8b). Softening of Raman bands at higher temperature is expected due to the anharmonicity involved in the atomic vibration mode. The first order temperature coefficient, χ, of this band, obtained from the linear relationship between frequency ω and temperature T, is found to be −0.018(3) cm^{-1} K^{-1}. The disappearance of the band around 350 K, can be attributed to the structural transition of the system to the higher symmetry cubic phase. Pure PZT-based systems are reported to transform from tetragonal to cubic phase (sp. group *Pm3m*) [24,50]. Around 380 K. In the cubic phase, the irreducible representation of optical phonon is: $\Gamma_{opt} = 3F_{1u} + F_{2u}$, where F_{1u} phonon is only infrared active and F_{2u} phonon is inactive both in Raman and infrared spectra. Therefore, in principle, in the high-temperature cubic phase, one can expect a complete absence of first-order Raman bands. The observation of broad Raman bands at 573 and 715 cm^{-1} at high temperature (> 350 K) is expected due to violation of Raman selection rules due to the cationic substitutional disorder which in turn likely to have a substantial contribution from phonon density of states. It can also be understood from the point of view of symmetry breaking in nano length scale due to the presence of polar-nano regions which is often originated in a substituted system to maintain the charge neutrality and chemical strain in a nanoscale region [53]. A possible discussion on PNRs related to spectral intensity is presented below.

We have also examined dependencies of the total intensity of Raman spectra on the temperature. The actual Raman intensity of the experimentally recorded Raman spectra are obtained by eliminating the thermal population factor using Bose-Einstein distribution function;

$$I(\omega) = \frac{I(\omega)_{0bs}}{(1 + n(\omega, T))} \tag{6}$$

where, $n(\omega) = \frac{1}{exp\left[\frac{\hbar\omega}{k_B T}\right] - 1}$ and I_{obs} is the experimental Raman intensity and n(ω,T) is the phonon population factor, ℏ is reduced plank's constant and k_B is the Boltzmann constant. The average intensity of each
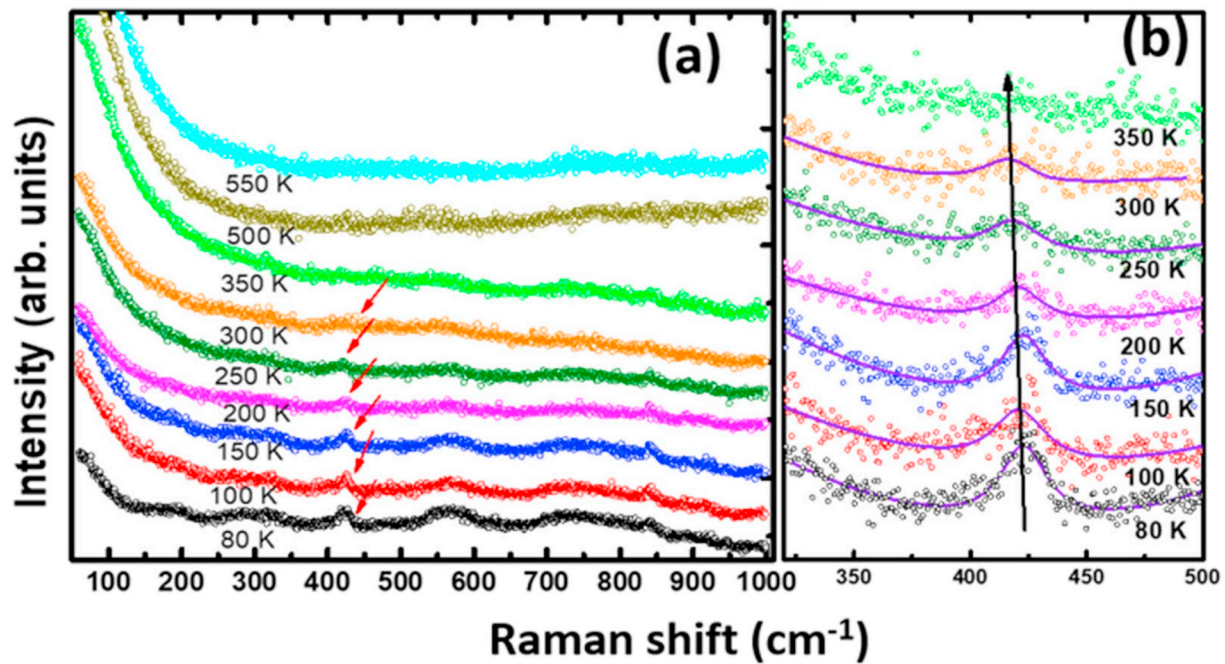
Fig. 8. (a) Raman spectra measured as a function of temperature in the *T*-range 80–550 K. Arrow mark indicates the temperature evolution of the E(LO$_2$) optical mode at 430 cm^{-1} and (b) Softening of E(LO$_2$) mode with temperature which vanishes in the cubic phase above 350 K.
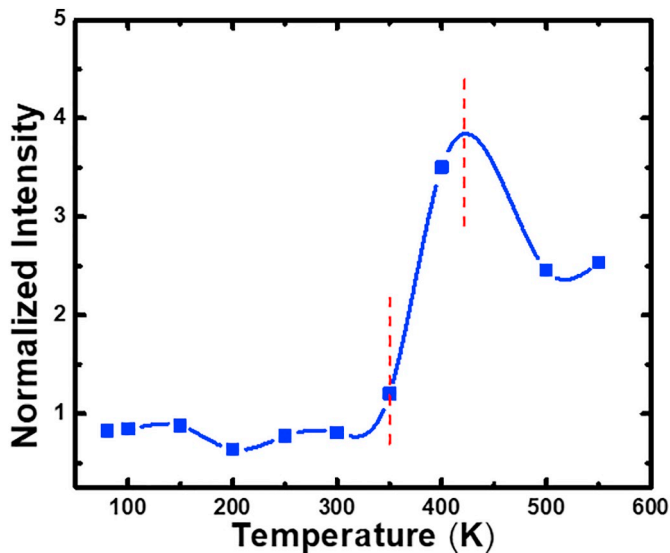

Fig. 9. Dependence of the normalized intensity of Raman spectra as a function of temperature in PZTS. Vertical lines indicate the tetragonal to cubic phase transition around 350 K, and ferroelectric to relaxor cubic phase transition above 400 K.

spectrum was obtained by integrating the Raman intensity in the spectral range 60–1000 cm^{-1}. To remove the effect of extrinsic factors such as optical alignment, focusing and laser power, a Raman spectrum was measured from the sample keeping the sample outside the cooling stage in the same spectral range as a reference spectrum. The total intensity of the spectrum was also obtained by integrating the spectrum in the same spectral range. Fig. 9 shows the total Raman intensity as a function of temperature after normalizing with respect to that of from bare sample. One can see the intensity show an anomaly at around 350 K, the tetragonal-cubic phase transition temperature. Since the tetragonality (*c/a*-1) in the system is only 0.005, [24] one can expect a transition to the higher symmetry cubic phase upon increasing temperature. The fact that the intensity falls rapidly above 450 K, pointing

towards its possible transition to a relaxor phase. Often the coupling of light in the ferroelectric system is considered from its order parameter (polarization Q) involved in the ferroelectric ordering and study on spectral intensity is useful in study of polar nanoregions (PNRs) [53]. Therefore, the sudden reduction in Raman intensity in cubic relaxor phase is due to random orientation of polarization originating from PNRs is understandable. This is what we exactly find from our dielectric spectroscopic studies, above 450 K also (discussed above). It can be mentioned here that for PZT based ferroelectric system, the tetragonality distortion disappears and the system transforms to a cubic phase before the ferroelectric to relaxor phase transition occurs above 600 K [50].

3.4. Ferroelectricity, and energy density calculations

In order to demonstrate the existence of ferroelectricity at nanoscale, the PZTS films were probed by piezoresponse force microscopy (PFM) at randomly selected areas. Fig. S2 shows amplitude and phase of PFM images of a MgO/LSMO/PZTS thin film obtained after polling $6 \times 6 \, \mu m^2$ area by -12 V and then subsequently the central $4 \times 4 \, \mu m^2$ area was poled by $+12$ V bias. A random polarization orientation was found in a grown film, whereas polarizations could be switched easily with a positive and negative bias.

Fig. 10 shows the *P-E* hysteresis loops of PZTS thin film measured at the various applied field. The slim loop of thin films capacitors suggesting relaxor ferroelectric behaviors of PZTS thin films in line with dielectric and Raman results. The remnant polarization (P_r) and coercive field (E_c) were found to increase with an increase in applied voltages (Fig. 10a). Near the breakdown electric field (~1.82 MV/cm), the P_r ~35.1 $\mu C/cm^2$ and E_c ~17.2 kV/cm, are obtained at 2 kHz and as expected these observed values of P_r and E_c are smaller than the undoped PZT [54–56]. We observed asymmetries of the hysteresis loop of Pt/PZTS/LSMO in the positive and negative branch could be due to different work functions [57] of the top and bottom electrodes. Choi et al. have reported symmetric hysteresis loop for same types of positive and negative electrodes, and asymmetric hysteresis loop of LSCO/PZT/LSCO, the different work functions of top and bottom electrodes lead to asymmetric polarization behaviors [58]. Besides this, defect-related
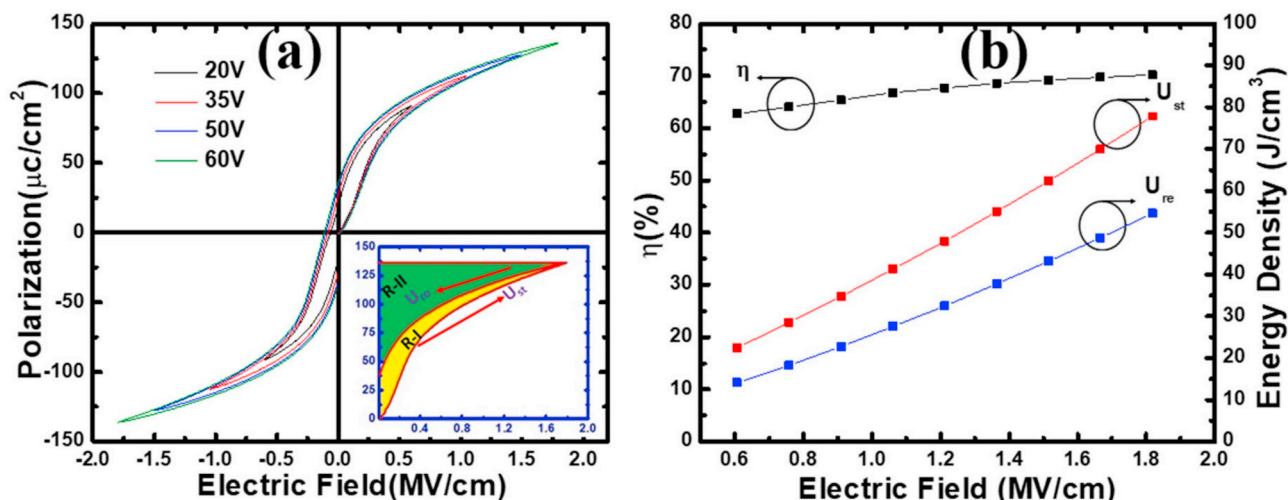
Fig. 10. (a) *P-E* hysteresis loops of PZTS thin films measured at various applied field at frequency 2 kHz (inset: *P-E* loops and energy density calculation at a higher electric field for LSMO/PZTS/Pt thin films capacitor (b) Efficiency and energy density of LSMO/PZTS/Ni thin films under various electric field.

Table 3
High energy density and efficiency of various thin films composition.

Material composition	U_{re} (J/cm^3)	η (%)	Electric field (MV/cm)	Worked by
BT/BST	12.24	67	1.65	Ortega et al. [8]
PLZT	13.7	88	1 kV/cm	Nguyen et al. [62]
PLZT/LNO	22	77	1.96	Tong et al. [63]
PLZT	30	78	2.18	Hu et al. [64]
PLZT	28.7	57	2.17	Hao et al. [19]
BZT	30.4	82	3	Zixiong et al. [65]
BCZT	8.23		3.8	Zhongbin et al. [66]
BZ/BT-BMT/PZ	28.36		0.75	Chen et al. [67]
PZTS	54.2	70	1.82	Present work

oxygen vacancy, impurities, and layer interface effect which act as pinning centered could also be responsible for the observed asymmetries hysteresis loop [59,60]. For the highest applied field, the remnant polarization (P_r) ~19.6 μC/cm^2 & coercive field (E_c) 60.2 KV/cm was reported for the Pt/PZT/Si (111) films grown using PLD technique [61].

Using the energy density formalism as discussed in the introduction, the recoverable energy density, U_{re}, for Pt/PZTS/LSMO thin films were estimated. It turns out to be ~54 J/cm^3, with a higher energy efficiency ~70% at an applied electric field 1.82 MV/cm and frequency 2 kHz. The obtained U_{re} and efficiency η in our PZTS thin films for several applied electric field are exhibited in Fig. 10(b). The studies on oriented Pb(Zr$_{0.52}$Ti$_{0.48}$)O$_3$(PZT) thin films, showed U_{re} ~8 J/cm^3 and η ~79.6% under applied electric field 0.8 MV/cm, synthesized by chemical solution method [68]. On the other hand, Nguyen et al. have reported [62] enhanced recoverable high energy density of 13.7 J/cm^3 and a high energy efficiency of 88.2% at 1 kV/cm in 10% La-doped epitaxial PLZT thin films grown on SRO/STO/Si substrates using pulsed laser deposition. U_{re} and η of the PLZT thin films are ~30 J/cm^3 ~78% at 2.18 MV/cm reported by Hu et al. [64]. In a similar research on PLZT thin films, U_{re} value was reported as 28.7 J/cm^3 with efficiency ~57% [19]. In the earlier report, for Pt/BT/BST grown thick films on MgO (001), Ortega et al. demonstrated from their extrapolate data, max U_{re} could be achieved 46 J/cm^3 with efficiency 75% [8]. Chen et al. achieved U_{re} value 28.36 J/cm^3 at 0.75 MV/cm for PZ/BT-BMT/PZ trilayer thin films. A comparison of our present results with other reported values on several thin films; U_{re} and η values are presented in Table 3.

4. Conclusions

Highly oriented (100) scandium substituted PZT epitaxial thin films on MgO substrate coated with LSMO were grown after optimization of processed parameters. Thin films were stabilized in a single tetragonal phase as inferred from XRD results. Six prominent Raman bands located at 294, 425, 481, 573, 715, and 786 cm^{-1} are identified by analyzing the ambient spectrum and are assigned. The symmetric and distinct E (LO$_2$) Raman band soften at elevated temperature with its intensity continuously decreases and vanishes in the cubic phase above 350 K. Existence of broad Raman bands at 573 and 715 cm^{-1} at high temperature (> 350 K is attributed to symmetry forbidden Raman scattering due to symmetry breaking in nano length scale in relaxor cubic phase. The dielectric, electrical and ferroelectric measurements carried out on LSMO/PSZT/Pt metal-ferroelectric-metal capacitors on a broader temperature range and frequencies suggests it relaxor behavior with a diffuse phase transition around 450 K. At room temperature, a high dielectric constant (ε′) ~5700 and low loss tangent ~0.01 were found at 100 Hz. Evidence of nanodomain switching of polarizations under external bias field was perceived on piezoelectric force microscopy measurement. We observed a remnant polarization ~35.1 μC/cm^2 and a low coercive field ~17.2 kV/cm, with a slim loop hysteresis for PZTS thin films corroborating its relaxor behavior. Using the data on hysteresis loop, an excellent high energy storage density (U_{re}) ~54 J/cm^3 with efficiency ~70% were estimated. High breakdown strength, larger dielectric constant and excellent estimated energy density ~54 J/cm^3 with efficiency ~70% of our thin films suggest its possible application into efficient energy storage capacitors.

Declaration of Competing Interest

The authors declare no competing financial interest.

Appendix A. Supplementary data

Supplementary data to this article can be found online at https://doi.org/10.1016/j.apsusc.2019.05.357.

References

[1] S.A. Sherrill, P. Banerjee, G.W. Rubloff, S.B. Lee, High to ultra-high power electrical energy storage, Phys. Chem. Chem. Phys. 13 (2011) 20714.

[2] N. Abas, A. Kalair, N. Khan, Review of fossil fuels and future energy technologies, Futures 69 (2015) 31–49.

[3] H. Yang, F. Yan, Y. Lin, T. Wang, Enhanced recoverable energy storage density and high efficiency of SrTiO3-based lead-free ceramics, Appl. Phys. Lett. 111 (2017).

[4] Z. Yang, H. Du, S. Qu, Y. Hou, H. Ma, J. Wang, J. Wang, X. Wei, Z. Xu, Significantly enhanced recoverable energy storage density in potassium–sodium niobate-based lead free ceramics, J. Mater. Chem. A 4 (2016) 13778–13785.

[5] A. Kumar, S.H. Kim, M. Peddigari, D.-H. Jeong, G.-T. Hwang, J. Ryu, High energy storage properties and electrical field stability of energy efficiency of (Pb0.89La0.11)(Zr0.70Ti0.30)0.9725O3 relaxor ferroelectric ceramics, Electron. Mater. Lett. 5 (2019) 323–330.

[6] M. Sharifzadeh Mirshekarloo, K. Yao, T. Sritharan, Large strain and high energy storage density in orthorhombic perovskite (Pb0.97La0.02) (Zr1-x-ySnxTiy) O3antiferroelectric thin films, Appl. Phys. Lett. 97 (2010) 3–6.

[7] C.W. Ahn, G. Amarsanaa, S.S. Won, S.A. Chae, D.S. Lee, I.W. Kim, Antiferroelectric thin-film capacitors with high energy-storage densities, low energy losses, and fast discharge times, ACS Appl. Mater. Interfaces 7 (2015) 26381–26386.

[8] N. Ortega, A. Kumar, J.F. Scott, D.B. Chrisey, M. Tomazawa, S. Kumari, D.G.B. Diestra, R.S. Katiyar, Relaxor-ferroelectric superlattices: high energy density capacitors, J. Phys. Condens. Matter. 24 (2012) 445901.

[9] G.A. Samara, Relaxor properties of compositionally disordered perovskites: Ba- and Bi-substituted Pb(Zr1-xTix)O3, Phys. Rev. B - Condens. Matter Mater. Phys. 71 (2005) 1–8.

[10] Z. Kutnjak, J. Petzelt, R. Blinc, The giant electromechanical response in ferroelectric relaxors as a critical phenomenon, Nature 441 (2006) 956–959.

[11] D.A. Sanchez, A. Kumar, N. Ortega, R.S. Katiyar, J.F. Scott, Near-room temperature relaxor multiferroic, Appl. Phys. Lett. 97 (2010) 21–24.

[12] A.A. Instan, S.P. Pavunny, M.K. Bhattarai, R.S. Katiyar, Ultrahigh capacitive energy storage in highly oriented Ba(ZrxTi1-x)O3 thin films prepared by pulsed laser de-position, 142903 (2017) 0–4.

[13] Z. Liang, M. Liu, C. Ma, L. Shen, L. Lu, C.L. Jia, High-performance BaZr0.35Ti0.65O3 thin film capacitors with ultrahigh energy storage density and excellent thermal stability, J. Mater. Chem. A. 6 (2018) 12291–12297.

[14] P. Gonnard, M. Troccaz, Dopant distribution between A and B sites in the PZT ceramics of type ABO3, J. Solid State Chem. 23 (1978) 321–326.

[15] E. Brown, C. Ma, J. Acharya, B. Ma, J. Wu, J. Li, Controlling dielectric and relaxor-ferroelectric properties for energy storage by tuning Pb0.92La0.08Zr0.52Ti0.48O3 film thickness, ACS Appl. Mater. Interfaces 6 (2014) 22417–22422.

[16] U. Balachandran, D.K. Kwon, M. Narayanan, B. Ma, Development of PLZT di-electrics on base metal foils for embedded capacitors, J. Eur. Ceram. Soc. 30 (2010) 365–368.

[17] G. Hu, C. Ma, W. Wei, Z. Sun, L. Lu, S.-B. Mi, M. Liu, B. Ma, J. Wu, C. Jia, Enhanced energy density with a wide thermal stability in epitaxial Pb0.92La0.08Zr0.52Ti0.48O3 thin films, Appl. Phys. Lett. 109 (2016) 193904.

[18] D. Mukherjee, M. Hordagoda, D. Pesquera, D. Ghosh, J.L. Jones, P. Mukherjee, S. Witanachchi, Enhanced ferroelectric polarization in epitaxial (Pb1-xLax)(Zr0.52Ti0.48)O3 thin films due to low La doping, Phys. Rev. B 95 (2017) 1–11.

[19] X. Hao, Y. Wang, J. Yang, S. An, J. Xu, High energy-storage performance in Pb0.91La0.09(Ti0.65Zr0.35)O3 relaxor ferroelectric thin films, J. Appl. Phys. 112 (2012) 114111.

[20] M. Tang, C. Ren, C. Tan, X. Zhong, Y. Tang, L. Gong, J. Wang, M. Liao, H. Guo, Highly transparent, all-oxide, heteroepitaxy ferroelectric thin film for flexible electronic devices, Appl. Surf. Sci. 458 (2018) 540–545.

[21] H. Zhu, H. Ma, Y. Zhao, Enhanced energy storage and pyroelectric properties of highly (100)-oriented (Pb1-x-yLaxCay)Ti1-x/4O3 thin films derived at low tem-perature, Phys. Lett. Sect. A Gen. At. Solid State Phys. 382 (2018) 1409–1412.

[22] N. Sun, Y. Li, Q. Zhang, X. Hao, Giant energy-storage density and high efficiency achieved in (Bi0.5Na0.5)TiO3-Bi(Ni0.5Zr0.5)O3 thick films with polar nanoregions, J. Mater. Chem. C 6 (2018) 10693–10703.

[23] W.-I. Lee, J.-K. Lee, II-S. Chung, C.-W. Chung and I.-K. Yoo, US Patent, 5, 625, 529, (1997).

[24] M.K. Bhattarai, S.P. Pavunny, A.A. Instan, J.F. Scott, R.S. Katiyar, Effect of off-center ion substitution in morphotropic lead zirconate titanate composition, J. Appl. Phys. 121 (2017) 194102.

[25] V. Marinova, B. Mihailova, T. Malcherek, C. Paulmann, K. Lengyel, L. Kovacs, M. Veleva, M. Gospodinov, B. Güttler, R. Stosch, U. Bismayer, Structural, optical and dielectric properties of relaxor-ferroelectric Pb0.78Ba0.22Sc0.5Ta0.5O3, J. Phys. Condens. Matter 18 (2006).

[26] M. Correa, A. Kumar, R.S. Katiyar, Microstructure-Relaxor Property Relationship of Microstructure-Relaxor Property Relationship, vol. 0193, (2012).

[27] S.K. Ghosh, K. Mallick, B. Tiwari, E. Sinha, S.K. Rout, Relaxor-ferroelectric BaLnZT (Ln = La, Nd, Sm, Eu, and Sc) ceramics for actuator and energy storage application, Mater. Res. Express. 5 (2018).

[28] J.F. Scott, Dielectric breakdown, negative resistivity, depletion widths and the role of Bi in Strontium Bismuth Tantalate (SBT) devices, Integr. Ferroelectr. 19 (1998) 85–93.

[29] N. Waeselmann, B. Mihailova, B.J. Maier, C. Paulmann, M. Gospodinov, V. Marinova, U. Bismayer, Local structural phenomena in pure and Ru-doped 0.9PbZn1/3Nb2/3O3-0.1PbTiO3 near the morphotropic phase boundary as revealed by Raman spectroscopy, Phys. Rev. B - Condens. Matter Mater. Phys. 83 (2011) 1–13.

[30] T.J. Zhu, L. Lu, M.O. Lai, Pulsed laser deposition of lead-zirconate-titanate thin films and multilayered heterostructures, Appl. Phys. A Mater. Sci. Process. 81 (2005) 701–714.

[31] S.K. Pandey, A.R. James, R. Raman, S.N. Chatterjee, A. Goyal, C. Prakash, T.C. Goel, Structural, ferroelectric and optical properties of PZT thin films, Phys. B Condens. Matter 369 (2005) 135–142.

[32] Y. Tsau, Y. Chen, H. Cheng, I. Lin, Ferroelectric (Ba,Sr)TiO3 and Pb(Zr,Ti)O3 thin films prepared by pulsed laser deposition, 21 (2001) 1561–1564.

[33] N. Izyumskaya, Y.-I. Alivov, S.-J. Cho, H. Morkoç, H. Lee, Y.-S. Kang, Processing, structure, properties, and applications of PZT thin films, Crit. Rev. Solid State Mater. Sci. 32 (2007) 111–202.

[34] S. Kumari, N. Ortega, D.K. Pradhan, A. Kumar, J.F. Scott, R.S. Katiyar, Effect of thickness on dielectric, ferroelectric, and optical properties of Ni substituted Pb (Zr0.2Ti0.8)O3 thin films, J. Appl. Phys. 118 (2015) 184103.

[35] R. Ranjan, R. Kumar, B. Behera, R.N.P. Choudhary, Effect of Sm on structural, di-electric and conductivity properties of PZT ceramics, Mater. Chem. Phys. 115 (2009) 473–477.

[36] S. Dussan, A. Kumar, J.F. Scott, R.S. Katiyar, Magnetic effects on dielectric and polarization behavior of multiferroic hetrostructures, Appl. Phys. Lett. 96 (2010) 072904.

[37] M. Delgado, E.V. Colla, P. Griffin, M.B. Weissman, D. Viehland, Field dependence of glassy freezing in a relaxor ferroelectric, Phys. Rev. B - Condens. Matter Mater. Phys. 79 (2009) 10–13.

[38] C.J. Stringer, T.R. Shrout, C.A. Randall, High-temperature perovskite relaxor fer-roelectrics: a comparative study, J. Appl. Phys. 101 (2007).

[39] T. Maiti, R. Guo, A.S. Bhalla, Structure-property phase diagram of BaZrxTi1-xO3 system, J. Am. Ceram. Soc. 91 (2008) 1769–1780.

[40] W. Janbua, T. Bongkarn, T. Kolodiazhnyi, N. Vittayakorn, High piezoelectric re-sponse and polymorphic phase region in the lead-free piezoelectric BaTiO3-CaTiO3-BaSnO3 ternary system, RSC Adv. 7 (2017) 30166–30176.

[41] Z. Yu, R. Guo, A.S. Bhalla, Dielectric behavior of Ba(Ti1-xZrx)O3 single crystals, J. Appl. Phys. 88 (2000) 410–415.

[42] G.H. Jonker, On the dielectric curie-weiss law and diffuse phase transition in fer-roelectrics, Mater. Res. Bull. 18 (1983) 301–308.

[43] Z. Yao, H. Liu, Y. Liu, Z. Wu, M. Cao, H. Hao, High-temperature relaxor cobalt-doped (1-x) BiSc O3 -xPbTi O3 piezoelectric ceramics, Appl. Phys. Lett. 92 (2008) 1–4.

[44] H. Menasra, Z. Necira, A. Boutarfaia, Structural and relaxor behavior of Pb 0.95 (La, J. Mater. Sci. Eng. A. 3 (2013) 615–620.

[45] J.C. M'Peko, A.G. Peixoto, E. Jimenez, L.M. Gaggero-Sager, Electrical properties of Nb-doped PZT 65/35 ceramics: influence of Nb and excess PbO, J. Electroceram. 15 (2005) 167–176.

[46] T.-F. Zhang, X.-X. Huang, X.-G. Tang, Y.-P. Jiang, Q.-X. Liu, B. Lu, S.-G. Lu, Enhanced electrocaloric analysis and energy-storage performance of lanthanum modified lead titanate ceramics for potential solid-state refrigeration applications, Sci. Rep. 8 (2018) 396.

[47] X. Diez-betriu, J.E. Garcia, C. Ostos, A.U. Boya, D.A. Ochoa, L. Mestres, R. Perez, Phase transition characteristics and dielectric properties of rare-earth (La, Pr, Nd, Gd) doped Ba (Zr0.09Ti0.91)O3 ceramics, Mater. Chem. Phys. 125 (2011) 493–499.

[48] S.J. Kuang, X.G. Tang, L.Y. Li, Y.P. Jiang, Q.X. Liu, Influence of Zr dopant on the dielectric properties and Curie temperatures of Ba(ZrxTi1-x)O3(0 ≤ x ≤ 0.12) cera-mics, Scr. Mater. 61 (2009) 68–71.

[49] L.D. Vuong, P.D. Gio, N.T. Tho, T. van Chuong, Relaxor ferroelectric properties of PZT-PZN-PMnN ceramics, Indian J. Eng. Mater. Sci. 20 (2013) 555–560.

[50] M. Deluca, H. Fukumura, N. Tonari, C. Capiani, N. Hasuike, K. Kisoda, C. Galassi, H. Harima, Raman spectroscopic study of phase transitions in undoped morpho-tropic PbZr1-xTixO3, J. Raman Spectrosc. 42 (2011) 488–495.

[51] M.D. Fontana, H. Idrissi, G.E. Kugel, K. Wojcik, Raman spectrum in PbTiO3 re-examined: dynamics of the soft phonon and the central peak, J. Phys. Condens. Matter. 3 (1991) 8695–8705.

[52] K.K. Mishra, A.T. Satya, A. Bharathi, V. Sivasubramanian, V.R.K. Murthy, A.K. Arora, Vibrational, magnetic, and dielectric behavior of La-substituted BiFeO3-PbTiO3, J. Appl. Phys. 110 (2011) 1–12.

[53] B. Maier, B. Mihailova, C. Paulmann, J. Ihringer, M. Gospodinov, R. Stosch, B. Güttler, U. Bismayer, Effect of local elastic strain on the structure of Pb-based relaxors: a comparative study of pure and Ba- and Bi-doped PbSc0.5Nb0.5O3, Phys. Rev. B - Condens. Matter Mater. Phys. 79 (2009) 1–8.

[54] F.M. Pontes, E.R. Leite, M.S.J. Nunes, D.S.L. Pontes, E. Longo, R. Magnani, P.S. Pizani, J.A. Varela, Preparation of Pb(Zr,Ti)O3 thin films by soft chemical route, J. Eur. Ceram. Soc. 24 (2004) 2969–2976.

[55] W. Cao, G. Jiang, D. Liu, W. Huang, J. Wang, Y. Chang, B. Yang, Ferroelectric properties of Ag doped PbZr0.53Ti0.47O3 thin film deposited by sol–gel process, J. Mater. Sci. Mater. Electron. 30 (2018) 2592–2599.

[56] B.T. Liu, X.B. Yan, X. Zhang, C.S. Cheng, F. Li, F. Bian, Q.X. Zhao, Q.L. Guo, Y.L. Wang, X.H. Li, X.Y. Zhang, C.R. Li, Y.S. Wang, Barrier performance of ultrathin Ni-Ti film for integrating ferroelectric capacitors on Si, Appl. Phys. Lett. 91 (2007) 3–5.

[57] M.& M. Toda, Asymmetric hysteresis loops, leakage current and capacitance voltage behaviors in ferroelectric PZT films deposited on a Pt/Al2O3/SiO2/Si substrate by MOCVD method with a vapor-deposited gold top electrode, Int. J. Appl. Phys. Math. 1 (2011) 3–7.

[58] C.H. Choi, J. Lee, B.H. Park, T.W. Noh, Asymmetric switching and imprint in (La,Sr)CoO3/Pb(Zr,Ti)O3/(La,Sr)CoO3 heterostructures, Integr. Ferroelectr. 18 (2007) 39–48.

[59] G. Singh, V.S. Tiwari, P.K. Gupta, Role of oxygen vacancies on relaxation and conduction behavior of KNbO3 ceramic, J. Appl. Phys. 107 (2010).

[60] R.E. Newnham, Properties of Materials: Anisotropy, Symmetry, Structure, Oxford University Press, 2005.

[61] S.K. Pandey, A.R. James, C. Prakash, T.C. Goel, K. Zimik, Electrical properties of PZT thin films grown by sol-gel and PLD using a seed layer, Mater. Sci. Eng. B Solid-State Mater. Adv. Technol. 112 (2004) 96–100.

[62] M.D. Nguyen, E.P. Houwman, M. Dekkers, C.T.Q. Nguyen, H.N. Vu, G. Rijnders, Research update: enhanced energy storage density and energy efficiency of epi-taxial $Pb_{0.9}La_{0.1}(Zr_{0.52}Ti_{0.48})O_3$ relaxor-ferroelectric thin-films deposited on silicon by pulsed laser deposition, APL Mater 4 (2016) 080701.

[63] S. Tong, B. Ma, M. Narayanan, S. Liu, R. Koritala, U. Balachandran, D. Shi, Lead lanthanum zirconate titanate ceramic thin films for energy storage, ACS Appl. Mater. Interfaces 5 (2013) 1474–1480.

[64] Z. Hu, B. Ma, S. Liu, M. Narayanan, U. Balachandran, Relaxor behavior and energy storage performance of ferroelectric PLZT thin films with different Zr/Ti ratios,

[65] Z. Sun, C. Ma, X. Wang, M. Liu, L. Lu, M. Wu, X. Lou, H. Wang, C.L. Jia, Large energy density, excellent thermal stability, and high cycling endurance of lead-free $BaZr_{0.2}Ti_{0.8}O_3$ film capacitors, ACS Appl. Mater. Interfaces 9 (2017) 17096–17101.

[66] Z. Pan, L. Yao, J. Zhai, H. Wang, B. Shen, Ultrafast discharge and enhanced energy density of polymer nanocomposites loaded with $0.5(Ba_{0.7}Ca_{0.3})TiO_3–0.5Ba(Zr_{0.2}Ti_{0.8})O_3$ one-dimensional nanofibers, ACS Appl. Mater. Interfaces 9 (2017) 14337–14346.

[67] T. Chen, J.B. Wang, X.L. Zhong, Y.K. Zeng, F. Wang, Y.C. Zhou, Improved energy storage properties of $PbZrO_3$ thin films by inserting $0.88BaTiO_3-0.12Bi(Mg_{1/2},Ti_{1/2})O_3$ layer, Appl. Surf. Sci. 285 (2013) 744–747.

[68] K.W. Lim, M. Peddigari, V. Annapureddy, G.T. Hwang, J.J. Choi, G.Y. Kim, S.N. Yi, J. Ryu, Energy storage characteristics of {001} oriented $Pb(Zr_{0.52}Ti_{0.48})O_3$ thin film grown by chemical solution deposition, Thin Solid Films 660 (2018) 434–438.